Dalton Transactions

ROYAL SOCIETY OF CHEMISTRY

PAPER

View Article Online
View Journal | View Issue

Cite this: *Dalton Trans.*, 2025, **54**, 15441

Two sites, two stories: sequence-driven divergence in Cu(II) and Zn(II) binding to CusF

Michał Pakowski and Aleksandra Hecel *

Copper homeostasis is a fine balance for bacteria: essential for respiration, yet toxic in excess. While the CusCFBA efflux system exports Cu(I) from Gram-negative cells, little is known about how its periplasmic chaperone, CusF, might respond to Cu(II) under oxidative stress. This study explored whether CusF's coordination environment is more adaptable than previously assumed, and how histidine spacing influences metal selectivity. We examined two peptides that mimic CusF metal-binding domains: a rare –HHH– motif (Ac-$_{22}$ANEHHHETMSE$_{32}$-NH$_2$) and a His/Met-rich binding site (Ac-$_{55}$TIHHDPIAAVNWPEMTMRFTITPQTKMSE$_{83}$-NH$_2$). Potentiometry, UV-Vis and CD spectroscopy, ESI-MS, and steady-state fluorescence were used to characterize their Cu(II) and Zn(II) complexes. At physiological pH, both peptides form Cu(II) species with a [1N$_{im}$, 2N$^-$] donor set. The –HHH– motif peptide stabilizes these complexes more effectively, likely due to earlier amide engagement enabled by its compact histidine triad. Zn(II) binds to the –HHH– motif peptide through three imidazole donors, whereas the His/Met-rich metal binding site shows higher overall Zn(II) affinity despite involving only two imidazoles. Fluorescence reveals metal-induced perturbations near tryptophan in the Ac-$_{55}$TIHHDPIAAVNWPEMTMRFTITPQTKMSE$_{83}$-NH$_2$, with Cu(II) causing stronger quenching and a larger red-shift than Zn(II). Comparison with a calcitermin-derived HxHxH peptide indicates that compact histidine –HHH– clustering better stabilizes Cu(II), whereas spaced histidines favor Zn(II), underscoring how sequence architecture governs metal selectivity.

Received 25th July 2025,
Accepted 24th September 2025

DOI: 10.1039/d5dt01770j

rsc.li/dalton

Introduction

Copper is an essential trace element that plays a critical role in both structural and catalytic cellular processes. However, its intracellular concentration must be tightly regulated, as imbalances, either deficiency or excess, can severely disrupt biochemical pathways, impair respiration, and ultimately lead to cell death.[1,2] In response to varying environmental conditions, bacteria have evolved sophisticated homeostatic and resistance mechanisms that ensure precise control over copper ion levels. Due to differences in cell wall architecture, Gram-positive and Gram-negative bacteria have developed distinct strategies for copper uptake and export.[3]

The uptake of Cu(II) ions from the environment and their transport into the periplasmic space across the outer membrane of Gram-negative bacteria occurs through three universal systems.

The first of these involves porins, which facilitate the passive transport of copper(II) ions. Examples of porins responsible for Cu(II) transport include OmpF and OmpC.[4–6] The second system involved in copper ion uptake consists of TonB-dependent transporters. Structurally, these transporters resemble proteins responsible for zinc ion acquisition. Members of this group include NosA, OprC, BtuB, TutA, FepA, and FhuA.[7] The OprC protein exhibits high selectivity towards Cu(II) ions, enabling their binding within a tetrahedral geometry involving a characteristic CXXXM-HXM sequence motif.[8] The OprC protein exhibits high selectivity toward copper ions, with binding occurring at the characteristic CXXXM-HXM motif. Structural and spectroscopic studies have shown that this site can accommodate both Cu(I) and Cu(II), with methionine residues providing a soft donor environment favoring Cu(I), while Cu(II) can also bind and may undergo reduction at the same site. Additionally, OprC contains a unique pathway formed by eleven methionine residues, which may direct copper ions from the outer surface of the cell membrane toward the binding site located at the base of the transport channel.[9] The third copper transport system involves metallophores, low molecular weight organic compounds with a high affinity for metal ions.[10] This system is activated under conditions of limited metal availability in the environment. In response, the bacterium synthesizes and secretes metallophores into the extracellular space, where they chelate metal ions. The metal-metallophore complexes are then recognized by specific membrane transporters, through which they are imported into the periplasmic space, where the metal ions are

Faculty of Chemistry, University of Wroclaw, 50383 Wroclaw, Poland.
E-mail: aleksandra.hecel2@uwr.edu.pl

subsequently released. Although the mechanisms governing copper transport from the periplasm to the cytosol remain incompletely understood, certain inner membrane proteins have been identified. One such transporter is CcoA, a member of the Major Facilitator Superfamily (MFS), which mediates copper uptake into the cytoplasm, primarily for the assembly of cytochrome *c* oxidases.[11]

To prevent the toxic effects of copper ions and maintain their homeostasis, bacteria employ systems that enable the export of these ions from the cytosol to the extracellular environment.

This export function is carried out by various protein families, including P-type ATPases, ABC transporters, and members of the RND (Resistance-Nodulation-Division) family.

It is worth noting that these proteins are also involved in the homeostasis of other metal ions, such as zinc. The system responsible for removing copper ions from the cell is the Cus system, which is mainly found in Gram-negative bacteria, including *E. coli.*[12] This transporter belongs to the RND (Resistance-Nodulation-cell Division) family and the HME (Heavy Metal Efflux) subfamily, and is responsible for pumping Cu(I) and Ag(I) ions out of the cell.[13] The Cus system forms a tripartite protein complex, CusABC, which creates a transport channel spanning from the inner membrane, through the periplasmic space, to the outer membrane of the cell, along with the periplasmic chaperone CusF. The first component of this system is the CusA protein, which is responsible for binding copper ions from the cytosol and transferring them to the next protein of the system, CusB. The apo-CusA structure exists in a closed conformation; however, upon binding a metal ion, such as Cu(I), a complex is formed (*e.g.*, Cu(I)-CusA), which induces the opening of the protein's structure. The initial binding of Cu(I) by CusA involves three methionine residues. Crystal structures of CusA have revealed that, in addition to this primary binding site, there are four additional pairs of methionine residues located within the transmembrane and periplasmic domains. These residues also participate in the coordination and transport of copper ions through the interior of the protein.[13] Another component of the system is the adaptor protein CusB, which connects the inner membrane transporter (CusA) with the outer membrane channel (CusC). CusB is a periplasmic protein composed of four domains.[14] The N-terminal methionine triad in CusB provides a soft S-donor site that binds Cu(I) through three conserved methionine residues (M21, M36, and M38) in trigonal geometry.[15] The final component of the tripartite transport channel is CusC, a homotrimeric protein with a structure typical of efflux pumps located in the outer membrane of Gram-negative bacteria. Structural analyses have shown that CusC does not possess specific Cu(I)-binding sites, due to the distances between methionine residues being too great to allow effective coordination. Nevertheless, similar to CusB, the inner surface of the CusC channel contains numerous negatively charged residues that facilitate the passage of positively charged metal cations out of the cell.[16]

Studies on the CusAB complex have shown that trimeric CusA can associate with six CusB units, forming a funnel-like structure. It is likely that the methionine triad in CusB serves as the binding site for Cu(I) ions delivered by the periplasmic chaperone CusF, which represents another component of the CusABCF export system.[17] Its synthesis is regulated by the intracellular concentration of Cu(I) ions.[12] CusF participates in transport by binding free copper ions from the periplasmic space or by receiving them from the CopA transporter,[18] and subsequently delivering them to the CusB and CusC proteins.[19] According to structural studies, CusF consists of a five-stranded β-barrel. Cu(I) ions are bound by CusF through one histidine residue and two methionine residues, both oriented toward the interior of the protein structure.[20–23] Although CusF is known to specifically bind Cu(I) and Ag(I) *via* a Met_2His motif, its localization in the oxidizing environment of the periplasm prompted us to investigate its potential interaction with Cu(II). While Cu(I) is the predominant species under anaerobic conditions and is the primary substrate of the CusCFBA efflux system, Cu(II) can be present in the periplasm as a result of oxidative stress or the presence of oxidizing agents. Therefore, we sought to explore whether CusF is capable of binding Cu(II), which could provide new insights into the flexibility of its metal-binding site and its possible role in bacterial adaptation to fluctuating redox conditions.[24] Moreover, the study by Vergnes *et al.* demonstrates that copper stress, sensed *via* the CusSR two-component system, induces the expression of the MsrPQ methionine sulfoxide reductase system, which in turn maintains CusF functionality by repairing oxidized methionine residues. These results underscore that CusF is not only involved in copper trafficking under anaerobic conditions but also plays a critical role in copper homeostasis under oxidative stress, where Cu(II) is prevalent. Therefore, investigating CusF–Cu(II) interactions provides important insights into the broader scope of bacterial copper regulation.[25] In addition to Cu(II), Zn(II) was included in this study as a biologically relevant comparison metal. While not directly transported by the CusCFBA system, Zn(II) shares key coordination features with Cu(II), including affinity for histidine residues, yet differs in its redox-inert character and preferred coordination geometry. Investigating Zn(II) interactions with CusF-derived peptides thus provides a valuable baseline for understanding how sequence context influences metal ion selectivity, and how CusF distinguishes between closely related but functionally distinct metal ions under physiological conditions.

To probe the metal-binding capacity of CusF, we investigated two distinct regions of the protein: (i) the N-terminal peptide fragment (Ac-$_{22}$ANE**HHH**ETMSE$_{32}$-NH_2) contains a –HHH– motif, and (ii) a His/Met-rich region (Ac-$_{55}$TI**HH**DPIAA-VNWPEMTMRFTITPQTKMSE$_{83}$-NH_2). To characterize its Cu(II) and Zn(II) interactions, we employed a combination of potentiometric titrations, UV-Vis and circular dichroism (CD) spectroscopy, fluorescence and mass spectrometry (MS). This multi-technique approach allowed us to gain detailed insights into the metal-binding properties and coordination behavior

of both regions, shedding light on the structural flexibility and potential functional diversity of CusF in response to varying metal oxidation states.

Experimental

Materials

The peptides (Ac-ANE**HHH**ETMSE-NH_2 and Ac-TI**HH**DPIAAVNWPEMTMRFTITPQTKMSE-NH_2) were purchased from Karebay Biochem (certified purity: 98%) and were used as received. The samples for electrospray ionization mass spectrometry (ESI-MS) were prepared in extra pure methanol (Sigma-Aldrich)–water mixture. Cu(II) and Zn(II) perchlorates were high-purity products [$Cu(ClO_4)_2{\cdot}6H_2O$ from Sigma-Aldrich; $Zn(ClO_4)_2{\cdot}6H_2O$ from POCH]. The concentrations of their stock solutions were determined by inductively coupled plasma mass spectrometry. The 0.1 M NaOH solution (Sigma-Aldrich), which was free of carbonates, was standardized by using potentiometry with potassium hydrogen phthalate (Sigma-Aldrich). All of the samples were prepared with freshly double distilled water. The ionic strength (I) was adjusted to 0.1 M by the addition of $NaClO_4$ (Sigma-Aldrich). 20 mM phosphate buffer with pH 7.4 was prepared from a mixture of salts ($Na_2HPO_4{\cdot}2H_2O$ and $NaH_2PO_4{\cdot}2H_2O$ from POCH and EuroChem, respectively).

Potentiometric measurements

The stability constants for proton Cu(II) and Zn(II) complexes with two ligands were calculated from titration curves carried out over the pH range of 2–11 at 298 K and ionic strength 0.1 M $NaClO_4$. The total volume of the solution used was 3.0 cm^3. The potentiometric titrations were performed using a Dosimat 800 Metrohm Titrator connected to a Methrom 905 pH-meter and a Mettler Toledo pH in Lab Science electrode. The thermostabilized glass cell was equipped with a magnetic stirring system, a microburet delivery tube and an inlet–outlet tube for argon. Solutions were titrated with 0.1 M carbonate-free NaOH. The electrodes were calibrated daily for hydrogen ion concentration through titrating $HClO_4$ with NaOH using a total volume of 3.0 cm^3. The ligand concentration was 0.3 mM, and the metal-to-ligand ratios were 0.9 : 1. The exact concentrations and the purities of the ligand solutions were determined by the Gran method.[26] The standard potential and the slope of the electrode couple were computed by means of GLEE program.[27] The HYPERQUAD 2008 program was used for the stability constant calculations.[28] The speciation diagrams were computed with the HYSS program.[29] In addition, the experimental and fitted titration curves obtained for the studied systems are presented in SI (Fig. S1). Hydrolysis constants for metal ions were taken from the literature (Table S1).[30,31]

Mass spectrometry

High-resolution mass spectra were obtained on a Bruker compact QTOF (Bruker Daltonik, Bremen, Germany), equipped with electrospray ionization source with an ion funnel. The mass spectrometer was operated in the positive ion mode. The instrumental parameters were as follows: scan range m/z 100–2000, dry gas – nitrogen, temperature 453 K, and ion energy 5 eV. The capillary voltage was optimized to the highest S/N ratio and it was 4800 V. The samples were prepared in 1 : 1 MeOH : H_2O mixture at pH 6 with a M : L molar ratio 0.9 : 1, where $[ligand]_{tot}$ = 0.1 mM. The samples were infused at a flow rate of 3 μL min^{-1}. The instrument was calibrated externally with a Tunemix™ mixture (Bruker Daltonik, Germany) in quadratic regression mode. Data were processed by application of the Compass DataAnalysis 4.2 (Bruker Daltonik, Germany) program. The mass accuracy for the calibration was better than 5 ppm, enabling together with the true isotopic pattern (using SigmaFit) an unambiguous confirmation of the elemental composition of the obtained complex.

Spectroscopic studies

The absorption spectra were recorded on a Jasco-V730 spectrophotometer, in the range 200–800 nm, using a quartz cuvette with an optical path of 1 cm. Circular dichroism spectra were recorded on a Chirascan CD spectrometer in the 200–800 nm range, using a quartz cuvette with an optical path of 1 and 0.1 cm in the visible and near-UV range. The concentration of sample solutions used for spectroscopic studies was similar to those employed in the potentiometric experiment. The metal : ligand ratio was 0.9 : 1. All spectroscopic measurements were recorded in the pH range 3–11. The pH of the samples was adjusted with the appropriate amounts of $HClO_4$ and NaOH solutions. The ε (UV-Vis) and $\Delta\varepsilon$ (CD) values listed in the tables correspond to the individual complex species identified in the distribution diagrams and were extracted from spectra recorded at the pH values where the respective species is present at its maximum concentration. OrginPro 2016 was used to process and visualize the obtained spectra.

Fluorescence experiments were performed on an RF-6000 spectrofluorometer (Shimadzu). All samples were prepared in 20 mM phosphate buffer at pH 7.4. The final peptide concentration in each sample was 50 μM. Titrations were performed by the stepwise addition of increasing concentrations of Cu(II) and Zn(II) ions (0–2 equiv.). Fluorescence emission was recorded at 345 nm upon excitation at 295 nm.

Results and discussion

Mass spectrometric insights into the Cu(II) and Zn(II) binding stoichiometry of the Ac-$_{22}$ANEHHHETMSE$_{32}$-NH_2 and Ac-$_{55}$TIHHDPIAAVNWPEMTMRFTITPQTKMSE$_{83}$-NH_2 fragments of CusF

Electrospray ionization mass spectrometry (ESI-MS) confirmed the stoichiometry of the Cu(II) and Zn(II) complexes with the two studies peptides, Ac-ANEHHHETMSE-NH_2 and Ac-TIHHDPIAAVNWPEMTMRFTITPQTKMSE-NH_2. Table S2 lists the m/z values for the free ligands and their metal complexes. The most intense signals (m/z = 681.77, z = 2+ for Ac-

ANEHHHETMSE-NH_2; (Fig. S2A and Table S2A) m/z = 1145.55, z = 3+ for Ac-TIHHDPIAAVNWPEMTMRFTITPQTKMSE-NH_2) (Fig. S2B and Table S2B) corresponds to the free peptides. Only monomeric species were detected, indicating that both peptides form 1 : 1 metal to ligand (M : L) complexes. For Ac-ANEHHHETMSE-NH_2, the monomeric complexes $[CuL]^{2+}$ and $[ZnL]^{2+}$ were detected at m/z = 712.23 and 712.73, respectively (Fig. S2A and Table S2A). In the case of Ac-TIHHDPIAAVNWPEMTMRFTITPQTKMSE-NH_2, the corresponding $[CuL]^{3+}$ and $[ZnL]^{3+}$ complexes appeared at m/z = 1161.24 (Fig. S2B and Table S2B). No evidence of polynuclear or bis-complexes was found in either ESI-MS or potentiometric measurements, further supporting a 1 : 1 stoichiometry under the experimental conditions.

Determination of protonation constants for Ac-$_{22}$ANEHHHETMSE$_{32}$-NH_2 and Ac-$_{55}$TIHHDPIAAVNWPEMTMRFTITPQTKMSE$_{83}$-NH_2 peptides from CusF

Potentiometric titrations of the Ac-ANEHHHETMSE-NH_2 and Ac-TIHHDPIAAVNWPEMTMRFTITPQTKMSE-NH_2 peptides revealed six distinct deprotonation constants (pK_a) for each ligand. For Ac-ANEHHHETMSE-NH_2, the first three pK_a values, 3.89, 4.05, and 4.81, are assigned to the deprotonation of carboxylic groups from glutamic acid residues. The subsequent values, 5.34, 6.29, and 6.59, correspond to the ionization of histidyl side chains (Table 1A).

In the case of Ac-TIHHDPIAAVNWPEMTMRFTITPQTKMSE-NH_2, the first two pK_a values (4.01 and 4.22) are likewise attributed to glutamic acid residues, followed by two pK_a values (5.41 and 7.00) arising from the deprotonation of histidyl imidazole groups. The final two constants, 9.67 and 11.27, are associated with the basic side chains of lysine and arginine, respectively (Table 1B). The obtained values are consistent with those reported in the literature for similar peptide-based systems.[32–36] Notably, the arginine side chain displays an unusually low apparent pK_a compared to the canonical value (~12–12.5). In Ac-TIHHDPIAAVNWPEMTMRFTITPQTKMSE-NH_2 peptide, Arg is embedded in a predominantly hydrophobic and low-dielectric environment (...MTMRFTIT...). Such conditions disfavor the stabilization of the protonated guanidinium group and thus facilitate deprotonation. This effect provides a straightforward rationale for the lower pK_a value obtained in our calculations compared to the typical values reported in aqueous solution.[37,38] Consistent with this interpretation, Wyrzykowski *et al.* reported markedly reduced arginine side-chain pK_a values (9.75 and 10.55 at 25 °C) for arginine-rich Pin1-derived peptides, attributed to guanidinium-driven aggregation and microenvironmental effects.[39] By contrast, the deprotonation of the Asp residue itself could not be reliably determined. Although Asp is present in the sequence, its expected pK_a (~3.8) overlaps with those of the adjacent Glu residues (~4.0–4.2). Consequently, the corresponding equilibrium makes only a negligible contribution to the overall titration curve, and Hyperquad consistently rejected this constant as statistically insignificant. The absence of an Asp equilibrium in the fitted model should therefore be interpreted not as a lack of deprotonation, but as a consequence of the strong overlap between acidic residues and their very low individual populations under the studied conditions.[29,40,41]

Investigation of coordination behavior of Ac-$_{22}$ANEHHHETMSE$_{32}$-NH_2 and Ac-$_{55}$TIHHDPIAAVNWPEMTMRFTITPQTKMSE$_{83}$-NH_2 with Cu(II)

Potentiometric measurements revealed that Cu(II) starts interacting with the Ac-$_{22}$ANEHHHETMSE$_{32}$ peptide above pH 3.5 forming a $[CuH_2L]^+$ species in which the metal ion is likely coordinated by one imidazole nitrogen [$1N_{im}$] (Table 1A and Fig. 1A). The next complex species, [CuHL], predominates at pH 5.5 and is associated with coordination of a second imidazole nitrogen. This is evidenced by a significant decrease in the pK_a value for this species (5.10) compared to the free ligand (6.29) (Table 1A). The appearance of a positive band at 258 nm in the CD spectrum (Table 1A and Fig. 3A) confirms imidazole nitrogen coordination to the Cu(II) ion.[42] For the $[CuL]^-$ species, which predominates at pH 6.2, a [$2N_{im}$, $1N^-$] binding mode was assigned. The appearance of two additional bands in the CD spectrum at λ = 372 and λ = 655 nm, indicates the involvement of the amide nitrogen in the coordination sphere (Table 1A and Fig. 3A). This is further supported by a UV-Vis band at λ = 607 nm, consistent with the formation of a 3N complex (Table 1A and Fig. 2A).[43–45] The lack of changes in the UV-Vis spectrum for the subsequent $[CuH_{-1}L]^{2-}$ species (λ = 601 nm) suggests the same 3N coordination mode, in which the third non-coordinating histidine residue undergoes deprotonation. This conclusion is supported by the fact that the pK_a value of this histidyl group in the complex (6.50) remains essentially unchanged compared to that of the free ligand (6.59).[33,34,46] Coordination of the second amide nitrogen occurs in the $[CuH_{-2}L]^{3-}$ species (with maximum concentration at pH 8.7), where the appearance of a positive (641 nm) and negative band (512 nm) in the CD spectrum (Fig. 3A) confirms the formation of a [$2N_{im}$, $2N^-$] complex with square-planar geometry.[47,48] In the $[CuH_{-3}L]^{4-}$ species, a blue shift in the UV-Vis absorption band (589 nm → 523 nm) indicates coordination of a third amide nitrogen to the Cu(II) ion, displacing one histidine residue and yielding a [$1N_{im}$, $3N^-$] complex.

In case of Cu(II)-Ac-$_{55}$TIHHDPIAAVNWPEMTMRFTITPQTKMSE$_{83}$-NH_2 system, the first two complex species, $[CuH_3L]^{2+}$ and $[CuH_2L]^+$, result from deprotonation and the binding of copper ions to two histidyl residues (Table 1B and Fig. 1B). The coordination of a second imidazole nitrogen is confirmed by a significant decrease in the pK_a value for the $[CuH_2L]^+$ species (5.20), compared to the free ligand (7.00) (Table 1B). The next species, [CuHL], with a maximum concentration at pH 7.3, indicates the involvement of an amide nitrogen in metal binding, forming [$2N_{im}$, $1N^-$] complex. This is evidenced by the appearance of a charge transfer (CT) band (N^- → Cu(II)) in the CD spectrum at 295 nm (Fig. 3B). Coordination of a second amide nitrogen occurs in the $[CuL]^-$ complex, which reaches its maximum concentration at pH 8.4, as indicated by a new CD band at 335 nm (Table 1B and Fig. 3B). Additionally, this complex adopts a square planar geometry, confirmed by

Table 1 Deprotonation constants (pK_a) for (A) Ac-$_{22}$ANEHHHETMSE$_{32}$-NH$_2$ and (B) Ac-$_{55}$TIHHDPIAAVNWPEMTMRFTITPQTKMSE$_{83}$-NH$_2$. Stability constants (log β) for their Cu(II) complexes in aqueous solution of 4 mM $HClO_4$ with I = 0.1 M $NaClO_4$ at 25 °C. C_L = 0.3 mM; M : L molar ratio = 0.9 : 1

			UV-Vis		CD		
Species	Log β_{ijk}[a]	pK_a[b]	λ [nm]	ε [cm^{-1} M^{-1}]	λ [nm]	$\Delta\varepsilon$ [cm^{-1} M^{-1}]	Donors
(A) Ac-$_{22}$ANEHHHETMSE$_{32}$-NH$_2$							
$[H_6L]^{3+}$	30.97(4)	3.89 (E)					
$[H_5L]^{2+}$	27.08(4)	4.05 (E)					
$[H_4L]^{+}$	23.03(4)	4.81 (E)					
H_3L	18.22(4)	5.34 (H)					
$[H_2L]^{-}$	12.88(3)	6.29 (H)					
$[HL]^{2-}$	6.59(5)	6.59 (H)					
$[CuH_2L]^{+}$	17.64(2)						1N$_{im}$
CuHL	12.54(2)	5.10			258	0.33	2N$_{im}$
$[CuL]^{-}$	6.69(2)	5.85	607	443.5	259	2.24	2N$_{im}$, 1N$^-$
					372	0.47	
					655	0.90	
$[CuH_{-1}L]^{2-}$	0.19(2)	6.50	601	284.3	256	2.98	2N$_{im}$, 1N$^-$
					377	0.44	
					652	0.76	
$[CuH_{-2}L]^{3-}$	−7.84(4)	8.03	589	90.1	250	4.25	2N$_{im}$, 2N$^-$
					334	−0.74	
					512	−0.28	
					641	0.59	
$[CuH_{-3}L]^{4-}$	−17.02(4)	9.18	523	106.5	259	6.53	1N$_{im}$, 3N$^-$
					313	0.42	
					499	−1.27	
					652	0.97	
(B) Ac-$_{55}$TIHHDPIAAVNWPEMTMRFTITPQTKMSE$_{83}$-NH$_2$							
$[H_6L]^{3+}$	41.58(4)	4.01 (E)					
$[H_5L]^{2+}$	37.57(4)	4.22 (E)					
$[H_4L]^{+}$	33.35(4)	5.41 (H)					
H_3L	27.94(3)	7.00 (H)					
$[H_2L]^{-}$	20.94(2)	9.67 (K)					
$[HL]^{2-}$	11.27(2)	11.27 (R)					
$[CuH_3L]^{2+}$	32.00(3)				258		1N$_{im}$
$[CuH_2L]^{+}$	26.80(2)	5.20			258		2N$_{im}$
CuHL	20.21(3)	6.59			259	0.46	2N$_{im}$, 1N$^-$
					295	−0.40	
$[CuL]^{-}$	12.32(3)	7.89	553	103.4	261	1.14	2N$_{im}$, 2N$^-$
					299	−0.27	
					335	0.17	
					580	−0.39	
$[CuH_{-1}L]^{2-}$	3.43(4)	8.89	551	121.5	261	1.40	1N$_{im}$, 3N$^-$
					298	−0.16	
					325	0.17	
					564	−0.50	
$[CuH_{-2}L]^{3-}$	−5.94(4)	9.37	541	118.9	262	1.75	4N$^-$
					318	0.30	
					563	−0.70	
$[CuH_{-3}L]^{4-}$	−15.63(3)	9.69	541	117.5	262	2.35	4N$^-$
					316	0.43	
					564	−0.83	

[a] Constants are presented as cumulative log β_{jk} values. $\beta(H_jL_k) = [H_jL_k]/([H]^j[L]^k)$, in which [L] is the concentration of the fully deprotonated peptide. Cu(II) stability constants are presented as cumulative log β_{ijk} values. L stands for a fully deprotonated peptide ligand that binds Cu(II) ions: $\beta(M_iH_jL_k) = [M_iH_jL_k]/([M]^i[H]^j[L]^k)$, where [L] is the concentration of the fully deprotonated peptide. [b] pK_a values of the peptides were derived from cumulative constants: $pK_a = \log\beta(H_jL_k) - \log\beta(H_{j-1}L_k)$. For Cu(II) complexes: $pK_a = \log\beta(M_iH_j + 1L_k) - \log\beta(M_iH_jL_k)$.

positive CD band at 580 nm (Fig. 3B). The UV-Vis spectrum further supports this geometry by showing an absorption band at 553 nm (Fig. 2B), consistent with a 4N coordination mode involving two imidazole nitrogens and two deprotonated amide nitrogens ([2N$_{im}$, 2N$^-$] donor set). Replacement of one histidyl residue by a third coordinating amide occurs in the $[CuH_{-1}L]^{2-}$ complex. The presence of CT bands at 298 and 325 nm and a d–d Cotton effect at 564 nm in the CD spectrum suggest a [1N$_{im}$, 3N$^-$] binding mode (Fig. 3B). The 4N coordination environment is further supported by the UV-Vis absorption band at 551 nm (Fig. 2B). A shift of the UV-Vis absorption band to 541 nm (Fig. 2B) suggests the coordination of a fourth amide nitrogen, resulting in the formation of a [4N$^-$] complex in the $[CuH_{-2}L]^{3-}$ species (max concentration at pH 9.7). The

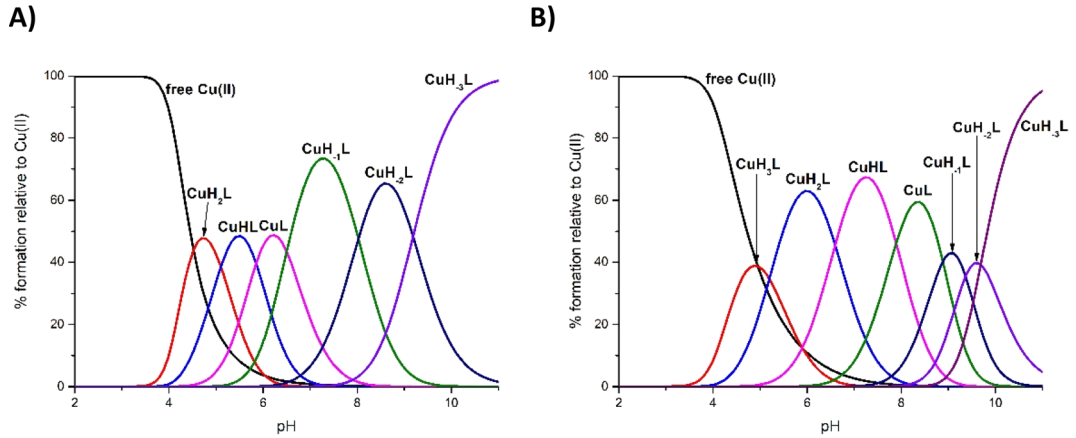

Fig. 1 Distribution diagrams for the formation of Cu(II) complex with (A) Ac-$_{22}$ANEHHHETMSE$_{32}$-NH_2 and (B) Ac-$_{55}$TIHHDPIAAVNWP-EMTMRFTITPQTKMSE$_{83}$-NH_2; T = 298 K and I = 0.1 M ($NaClO_4$), C_M = 0.3 × 10^{-3} M; M : L molar ratio = 0.9 : 1. For clarity, formal charges of the complex species are omitted in the figures; complete charge states are given in Table 1 and in the text.

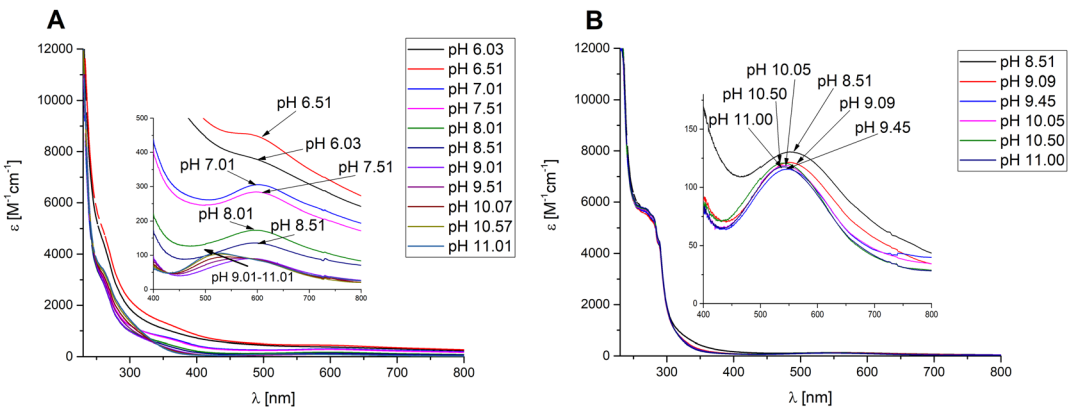

Fig. 2 pH-dependent UV-Vis absorption spectra for (A) Cu(II)-Ac-$_{22}$ANEHHHETMSE$_{32}$-NH_2 and (B) Cu(II)-Ac-$_{55}$TIHHDPIAAVNWPEMT-MRFTITPQTKMSE$_{83}$-NH_2 in aqueous solution of 4 mM $HClO_4$ with I = 0.1 M $NaClO_4$. Optical path length of 1 cm. C_L = 0.3 mM; M : L molar ratio = 0.9 : 1; T = 25 °C.

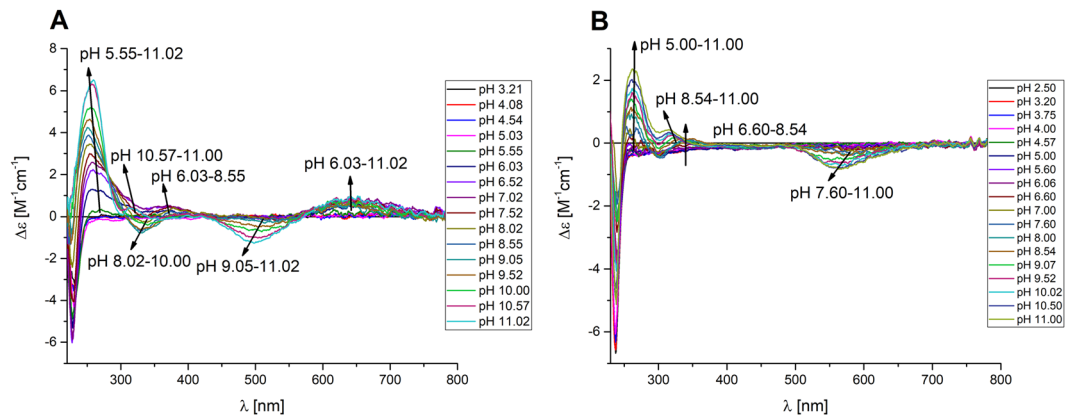

Fig. 3 pH-dependent CD spectra for (A) Cu(II)-Ac-$_{22}$ANEHHHETMSE$_{32}$-NH_2 and (B) Cu(II)-Ac-$_{55}$TIHHDPIAAVNWPEMTMRFTITPQTKMSE$_{83}$-NH_2 in aqueous solution of 4 mM $HClO_4$ with I = 0.1 M $NaClO_4$. Optical path length of 1 cm. C_L = 0.3 mM; M : L molar ratio = 0.9 : 1; T = 25 °C.

last species, $[CuH_{-3}L]^{4-}$, results from the deprotonation of a non-binding lysine residue, as evidenced by the unchanged pK_a value (9.69) compared to the free ligand (9.67) (Table 1B). The absence of spectral changes in both the UV-Vis and CD spectra further confirms the retention of the $4N^-$ coordination mode.

It is worth noting that pH-metric titrations of the Cu(II) complexes with both ligands, Ac-$_{22}$ANEHHHETMSE$_{32}$-NH$_2$ and Ac-$_{55}$TIHHDPIAAVNWPEMTMRFTITPQTKMSE$_{83}$-NH$_2$, led to the formation of a slight opalescent precipitate, completely invisible during mixing, in the pH range of 4.0–6.5 for the Cu(II)-Ac-$_{22}$ANEHHHETMSE$_{32}$-NH$_2$, and between pH 4.0–8.0 for the Cu(II)-Ac-$_{55}$TIHHDPIAAVNWPEMTMRFTITPQTKMSE$_{83}$-NH$_2$. This phenomenon resulted in a significantly elevated baseline in the UV-Vis spectra, preventing reliable identification of the very weak d–d transition bands typically observed for Cu(II) coordination environments. Importantly, this slight precipitation effect had no measurable influence on the CD spectra recorded over the same pH range, nor was it detected during potentiometric titrations. Nevertheless, due to the high sensitivity of UV-Vis spectroscopy to light-scattering phenomena, the opalescence was clearly visible in this technique and could have otherwise remained unnoticed using less sensitive analytical methods.

The observed opalescence likely results from local aggregation effects, particularly in the pH range where the net charge of the peptide approaches zero. This may be further influenced by the accumulation of positive charges from protonated side chains (*e.g.*, lysine, arginine, and non-coordinated histidines), which disturb electrostatic balance, reduce overall solubility, and promote peptide–peptide interactions.[33,34]

Study of coordination properties of Ac-$_{22}$ANEHHHETMSE$_{32}$-NH$_2$ and Ac-$_{55}$TIHHDPIAAVNWPEMTMRFTITPQTKMSE$_{83}$-NH$_2$ with Zn(II)

The first Zn(II)-Ac-$_{22}$ANEHHHETMSE$_{32}$-NH$_2$ species, $[ZnH_4L]^{3+}$ and $[ZnH_3L]^{2+}$, appear at low pH values and reach their maximum concentrations at pH 3.8 and 4.5, respectively. These complexes likely involve coordination through the carboxylate oxygens of glutamic acid residues (Table 2A and Fig. 4A). Subsequent deprotonation steps lead to the formation of $[ZnH_2L]^+$, ZnHL and $[ZnL]^-$ species, which are most likely associated with the stepwise coordination of three histidine residues. This is supported by the slightly lowered pK_a values of these forms (5.05, 6.09 and 6.10, respectively) compared to the free ligand (5.34, 6.29 and 6.59, respectively), indicating stabilization upon metal binding. The last species, $[ZnH_{-1}L]^{2-}$, with maximum concentration at pH 8.5, most likely corresponds to the formation of a hydroxylated complex [3N$_{im}$, 1OH$^-$].

For the second ligand, Ac-$_{55}$TIHHDPIAAVNWPEMTMRFTITPQTKMSE$_{83}$-NH$_2$, a similar coordination pattern is observed (Table 2B and Fig. 4B). The first species, $[ZnH_4L]^{3+}$, likely involves zinc binding to the carboxylic group of a glutamic acid residue. The appearance of $[ZnH_3L]^{2+}$ and $[ZnH_2L]^+$ species, with notably shifted pK_a values (4.40 and 5.00 *vs.* 5.41 and 7.00 for the free ligand), indicates participation of two histidine side chains in Zn(II) binding. The final two species, [ZnHL] and $[ZnL]^-$, reaching maximum concentrations at pH 7.5 and 10.0, respectively, are associated with the stepwise deprotonation of coordinated water molecules, leading to the formation of hydroxo complexes with proposed [2N$_{im}$, 1OH$^-$] and [2N$_{im}$, 2OH$^-$] binding modes.

Table 2 Stability constants (log β) for (A) Zn(II)-Ac-$_{22}$ANEHHHETMSE$_{32}$-NH$_2$ and (B) Zn(II)-Ac-$_{55}$TIHHDPIAAVNWPEMTMRFTITPQTKMSE$_{83}$-NH$_2$ complexes in aqueous solution of 4 mM $HClO_4$ with I = 0.1 M $NaClO_4$ at 25 °C. C_L = 0.3 mM; M : L molar ratio = 0.9 : 1

Species	Log β	pK_a	Donors
(A) Ac-$_{22}$ANEHHHETMSE$_{32}$-NH$_2$			
$[ZnH_4L]^{3+}$	27.15(4)		COO^-_{Glu}
$[ZnH_3L]^{2+}$	22.71(2)	4.44	COO^-_{Glu}
$[ZnH_2L]^+$	17.66(2)	5.05	1N$_{im}$
ZnHL	11.57(3)	6.09	2N$_{im}$
$[ZnL]^-$	5.47(2)	6.10	3N$_{im}$
$[ZnH_{-1}L]^{2-}$	−1.82(3)	7.29	3N$_{im}$, 1OH$^-$
(B) Ac-$_{55}$TIHHDPIAAVNWPEMTMRFTITPQTKMSE$_{83}$-NH$_2$			
$[ZnH_4L]^{3+}$	38.57(5)		COO^-_{Glu}
$[ZnH_3L]^{2+}$	34.17(3)	4.40	1N$_{im}$
$[ZnH_2L]^+$	29.17(4)	5.00	2N$_{im}$
ZnHL	22.91(4)	6.26	2N$_{im}$, 1OH$^-$
$[ZnL]^-$	14.98(5)	7.93	2N$_{im}$, 2OH$^-$

To better illustrate the coordination modes of the dominant species at physiological pH (~7.0), representative binding models were constructed using PyMol (Fig. 5). The structures are based on the major species identified in the speciation diagrams and supported by spectroscopic data. In the Cu(II)-Ac-$_{22}$ANEHHHETMSE$_{32}$-NH$_2$ system, the dominant $[CuH_{-1}L]^{2-}$ complex adopts a [2N$_{im}$, 1N$^-$] coordination mode, involving two histidine imidazole and one deprotonated backbone amide (Fig. 5A). A comparable binding pattern is observed for Cu(II)-Ac-$_{55}$TIHHDPIAAVNWPEMTMRFTITPQTKMSE$_{83}$-NH$_2$, where the major [CuHL] species also features a [2N$_{im}$, 1N$^-$] donor set (Fig. 5B). The $[ZnL]^-$ complex formed by Ac-$_{22}$ANEHHHETMSE$_{32}$-NH$_2$ involves coordination through all three histidine residues (Fig. 5C), while the [ZnHL] complex observed for TIH is best described as involving two imidazoles and a water molecule [2N$_{im}$, 1OH$^-$] (Fig. 5D). The resulting models highlight how subtle differences in histidine arrangement and peptide architecture influence donor selection, coordination geometry, and ultimately metal-binding preferences.

Structural properties of investigated metal binding sites and their Cu(II) and Zn(II) complexes

To investigate the structural features and conformational changes of the studied ligands upon metal coordination, CD spectra were recorded in the far-UV region (180–300 nm). The CD spectrum of the Ac-$_{55}$TIHHDPIAAVNWPEMTMRFTITPQTKMSE$_{83}$-NH$_2$ peptide is largely disordered throughout the studied pH range, exhibiting a single broad negative band centered around 197 nm, characteristic of a predominantly

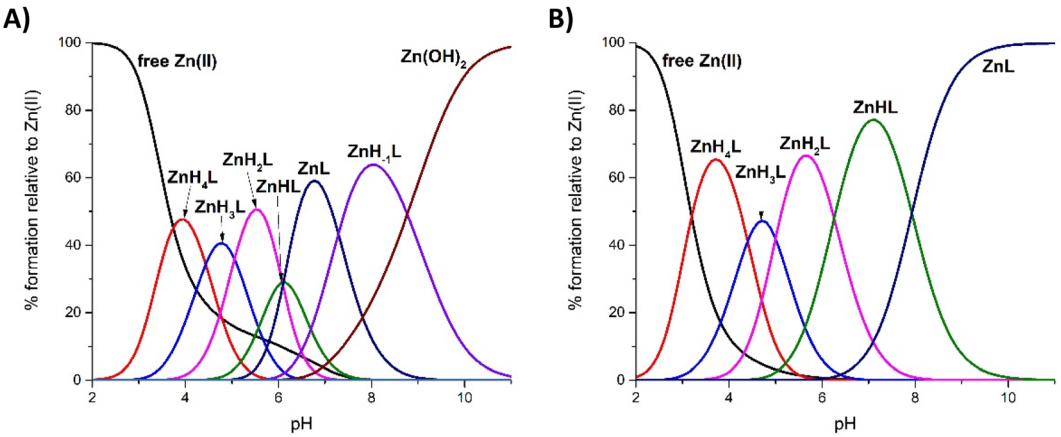

Fig. 4 Distribution diagrams for the formation of Zn(II) complex with (A) Ac-$_{22}$ANEHHHETMSE$_{32}$-NH$_2$ and (B) Ac-$_{55}$TIHHDPIAAVNWPEMTMRFTITPQTKMSE$_{83}$-NH$_2$; T = 298 K and I = 0.1 M ($NaClO_4$), C_M = 0.3 × 10^{-3} M; M : L molar ratio = 0.9 : 1. For clarity, formal charges of the complex species are omitted in the figures; complete charge states are given in Table 2 and in the text.

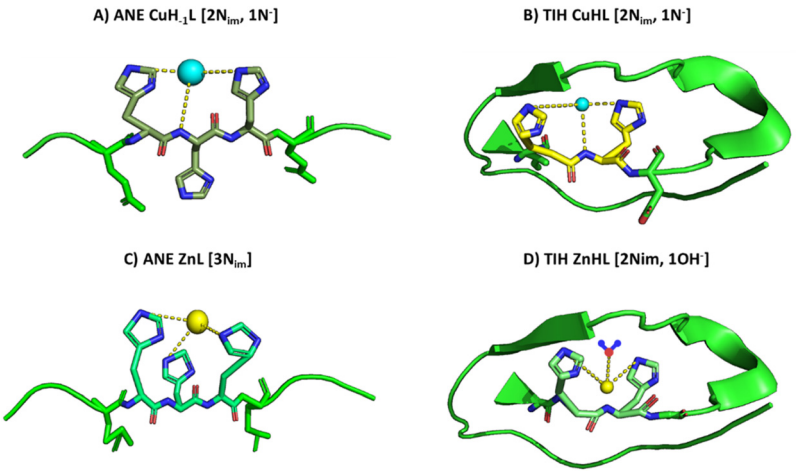

Fig. 5 PyMol models of the dominant Cu(II) and Zn(II) complexes formed by Ac-$_{22}$ANEHHHETMSE$_{32}$-NH$_2$ (ANE) and Ac-$_{55}$TIHHDPIAAVNWPEMTMRFTITPQTKMSE$_{83}$-NH$_2$ (TIH) peptides at physiological pH, based on potentiometric and spectroscopic data. (A) $[CuH_{-1}L]^{2-}$ complex of ANE, with a [2N$_{im}$, 1N$^-$] coordination mode; (B) [CuHL] complex of TIH, also adopting a [2N$_{im}$, 1N$^-$] donor set; (C) $[ZnL]^-$ complex of ANE, coordinated through three histidine imidazoles [3N$_{im}$]; (D) [ZnHL] complex of TIH, featuring two histidine imidazoles and one water molecule [2N$_{im}$, 1OH$^-$]. Metal ions are shown as spheres (cyan for Cu(II), yellow for Zn(II)); ligands are depicted as sticks, and peptide secondary structure is shown in cartoon representation. For clarity, formal charges of the complex species are omitted in the figures; complete charge states are given in Tables 1 and 2, and in the text. For clarity, the depicted amide donor is representative and does not correspond to a single, uniquely assigned residue.

random coil conformation (Fig. S3D). In contrast, the Ac-$_{22}$ANEHHHETMSE$_{32}$-NH$_2$ peptide displays a similar negative band near 200 nm in all pH range, but with increasing pH, the spectrum gradually develops an additional weak negative band around 225 nm (Fig. S3A). This spectral feature is indicative of a slight tendency toward α-helical folding, suggesting that the Ac-$_{22}$ANEHHHETMSE$_{32}$-NH$_2$ peptide may adopt a more ordered secondary structure under basic conditions.

Coordination of Cu(II) and Zn(II) ions to the Ac-$_{55}$TIHHDPIAAVNWPEMTMRFTITPQTKMSE$_{83}$-NH$_2$ does not induce significant changes in its secondary structure across the entire studied pH range, as evidenced by the far-UV CD spectra (Fig. S3E and F). At physiological pH (~pH 7), the spectra of the apo form and both metal complexes are nearly superimposable, each displaying a broad negative band centered around 197 nm, characteristic of a predominantly disordered conformation (Fig. 6B). These results suggest that metal binding does not impose conformational constraints on the Ac-$_{55}$TIHHDPIAAVNWPEMTMRFTITPQTKMSE$_{83}$-NH$_2$, indicating a lack of structural reorganization upon coordination. This behavior may reflect the inherent flexibility of the peptide backbone or the absence of a well-defined secondary structure in the vicinity of the metal-binding site.

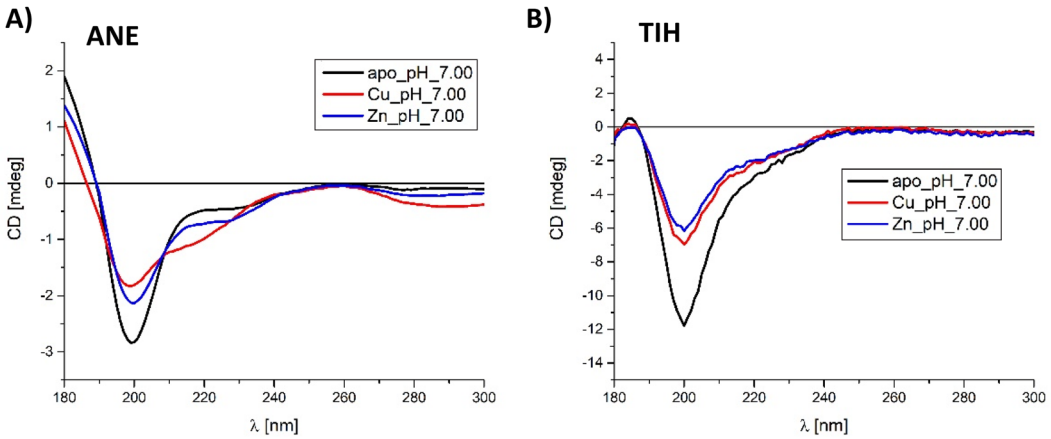

Fig. 6 CD spectra comparison between (A) Ac-$_{22}$ANEHHHETMSE$_{32}$-NH$_2$, (B) Ac-$_{55}$TIHHDPIAAVNWPEMTMRFTITPQTKMSE$_{83}$-NH$_2$ and its Cu(II) and Zn(II) complexes at pH 7 in aqueous solution of 4 mM $HClO_4$ with I = 0.1 M $NaClO_4$ at 25 °C. C_L = 0.1 mM; M : L molar ratio = 0.9 : 1.

In contrast to the His/Met-rich metal binding site peptide, the –HHH– motif peptide exhibits a pronounced structural response upon coordination with Cu(II) and Zn(II) ions. At pH 7, comparison of the apo peptide and its Cu(II) and Zn(II) complexes (Fig. 6A) reveals clear differences in the intensity and shape of the spectral features. For the Cu(II)-Ac-$_{22}$ANEHHHETMSE$_{32}$-NH$_2$ complex, CD spectra recorded at pH 3, 5 and 7 show a dominant negative band near 200 nm, accompanied by a weaker negative shoulder around 225 nm, consistent with partial α-helical content (Fig. S3B). However, at higher pH values (pH 9 and 11), a striking spectral transformation is observed. In addition to the negative bands near 200 and 220 nm, a new and distinct positive band emerges in the 240–260 nm region, indicating a significant conformational rearrangement, likely associated with changes in coordination geometry or peptide folding (Fig. S3B). For the Zn(II)-Ac-$_{22}$ANEHHHETMSE$_{32}$-NH$_2$ complex, the spectral evolution is more gradual but also indicative of increased structural ordering. The main negative band at 200 nm remains present across the pH range, while the band around 225 nm becomes progressively more pronounced with increasing pH (Fig. S3C), suggesting a stabilization of helical elements upon Zn(II) coordination under basic conditions.

Cu(II) and Zn(II) binding properties at two sites of CusF: a thermodynamic perspective

To gain deeper insight into the metal-binding properties of the two metal binding sites of CusF with Cu(II) and Zn(II), competition diagrams were plotted (Fig. 7). These diagrams, based on overall stability constants of the binary complexes, simulate equimolar conditions of ligands and metal ions in solution. They provide a clear comparison of the complexation tendencies of Ac-$_{22}$ANEHHHETMSE$_{32}$-NH$_2$ and Ac-$_{55}$TIHHDPIAAVNWPEMTMRFTITPQTKMSE$_{83}$-NH$_2$ peptides across the entire examined pH range. The results clearly show an inverse trend in metal ion binding: Ac-$_{22}$ANEHHHETMSE$_{32}$-NH$_2$ forms more stable complexes with Cu(II) across a broad pH range, while Ac-$_{55}$TIHHDPIAAVNWPEMTMRFTITPQTKMSE$_{83}$-NH$_2$ exhibits a much stronger affinity toward Zn(II). Importantly, in both peptides Cu(II) is coordinated by two histidine residues

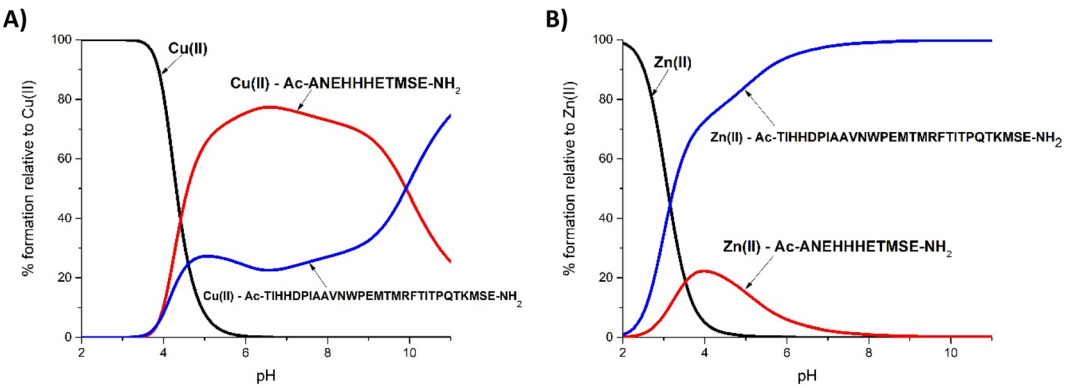

Fig. 7 Competition plots for a simulated solution containing equimolar concentrations of (A) Cu(II), (B) Zn(II), Ac-$_{22}$ANEHHHETMSE$_{32}$-NH$_2$ and Ac-$_{55}$TIHHDPIAAVNWPEMTMRFTITPQTKMSE$_{83}$-NH$_2$. The diagrams are calculated from the overall stability constants of the binary complexes and simulate a situation in which equimolar concentrations of all of the chosen ligands and metals are present in a solution.

together with deprotonated backbone amides. The higher stability of Ac-$_{22}$ANEHHHETMSE$_{32}$-NH_2 may arise from its –HHH– motif, which provides a compact arrangement of histidines that facilitates earlier backbone deprotonation and amide coordination, thereby stabilizing Cu(II) complexes at lower pH values, even though only two imidazoles are directly bound (Fig. 7A). This preorganization lowers the entropic cost of coordination and provides greater stability compared to the longer and more flexible His/Met-rich sequence. However, at alkaline pH (above 10), competition plots show that Ac-$_{55}$TIHHDPIAAVNWPEMTMRFTITPQTKMSE$_{83}$-NH_2 begins to surpass Ac-$_{22}$ANEHHHETMSE$_{32}$-NH_2 in Cu(II) complexation. This shift can be explained by the formation of a highly stable [$4N^-$] complex in Ac-$_{55}$TIHHDPIAAVNWPEMTMRFTITPQTKMSE$_{83}$-NH_2, involving four deprotonated amide nitrogens arranged in a square-planar geometry, which provides a thermodynamic advantage over the more compact Ac-$_{22}$ANEHHHETMSE$_{32}$-NH_2 fragment.

In contrast, Zn(II) complexes are more stable with the longer Ac-$_{55}$TIHHDPIAAVNWPEMTMRFTITPQTKMSE$_{83}$-NH_2 (Fig. 7B), even though only two histidine imidazole nitrogens are involved in coordination, compared to three in the Ac-$_{22}$ANEHHHETMSE$_{32}$-NH_2. This suggests that factors beyond the number of coordinating histidines contribute to Zn(II) binding affinity. The extended sequence of Ac-$_{55}$TIHHDPIAAVNWPEMTMRFTITPQTKMSE$_{83}$-NH_2 likely provides additional stabilization through secondary interactions involving backbone carbonyls, polar side chains, or a more flexible scaffold that better accommodates Zn(II)'s preferred tetrahedral or distorted octahedral geometry. In contrast, the compact –HHH– motif, while efficient for Cu(II) binding, may introduce steric constraints that reduce complex stability with Zn(II). Thus, while –HHH–motif peptide is better suited for Cu(II) coordination due to its densely packed histidine array, the longer and more conformationally versatile Ac-$_{55}$TIHHDPIAAVNWPEMTMRFTITPQTKMSE$_{83}$-NH_2 creates a more favorable coordination environment for Zn(II). Although Met/His-rich binding site contributes only two imidazole donors, its Zn(II) complexes are more stable than those of Ac-$_{22}$ANEHHHETMSE$_{32}$-NH_2, which coordinates through three histidines. This apparent paradox arises from donor identity and geometry rather than histidine count. TIH forms [$2N_{im}$, $1OH^-$ and $2N_{im}$, $2OH^-$] species that provide the preferred tetrahedral environment for Zn(II), and hydroxo ligation is more stabilizing than additional neutral imidazole donors. In contrast, Ac-$_{22}$ANEHHHETMSE$_{32}$-NH_2 stabilizes Zn(II) mainly with [$3N_{im}$] up to higher pH, introducing OH^- only later. The flexible Ac-$_{55}$TIHHDPIAAVNWPEMTMRFTITPQTKMSE$_{83}$-NH_2 sequence further facilitates tetrahedral geometry, while the compact –HHH– motif imposes steric constraints. Thus, the higher stability of Zn(II)-Ac-$_{55}$TIHHDPIAAVNWPEMTMRFTITPQTKMSE$_{83}$-NH_2 reflects early and efficient hydroxo coordination combined with favorable geometry, not simply the number of histidines.

Due to the intriguing coordination chemistry of three consecutive histidine residues (–HHH–), a relatively rare motif in natural proteins, the thermodynamic stability of this sequence was compared with that of a peptide derived from calcitermin, antimicrobial peptide, which features the HxHxH motif (Fig. 8).[49] Both peptides used in the comparison were N- and C-terminally protected to prevent end-group interference in metal binding. The rationale behind this comparison lies in the potential impact of histidine spacing on metal ion coordination geometry and complex stability. Notably, while the –HHH– motif provides three adjacent donor sites, the HxHxH arrangement introduces greater flexibility and potentially reduces steric hindrance. Understanding these subtle differences is essential for elucidating the principles governing metal–peptide interactions, particularly with biologically relevant metal ions such as Cu(II) and Zn(II).

The pH-dependent complex formation profiles of Cu(II) with two peptides Ac-VAILAKAAHYHTHKE-NH_2 and Ac-ANEHHHETMSE-NH_2 show distinct differences in their coordination behavior. Above pH 5, the calcitermin-derived peptide (Ac-VAILKAAHYHTHKE-NH_2) begins to form Cu(II) complexes that are thermodynamically more stable (Fig. 8A). These results indicate that histidine spacing significantly influences the thermodynamic stability and formation efficiency of Cu(II)–peptide complexes. The HxHxH motif in the calcitermin-

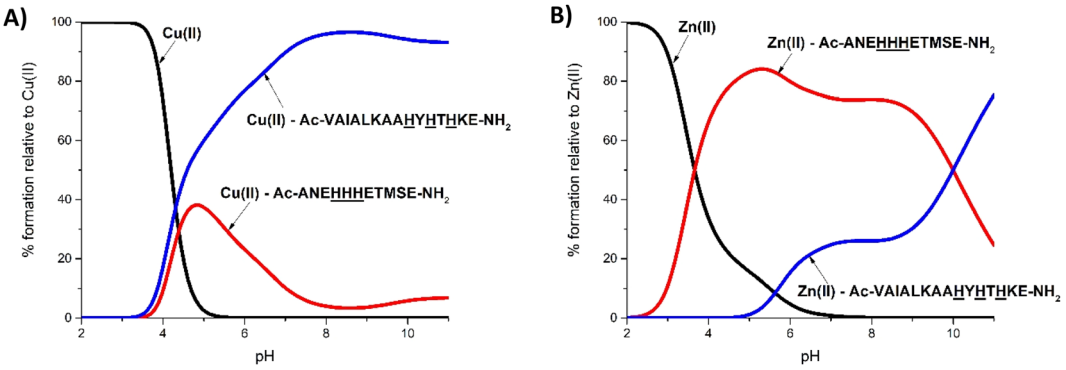

Fig. 8 Competition plots for a simulated solution containing equimolar concentrations of (A) Cu(II), (B) Zn(II), Ac-$_{22}$ANEHHHETMSE$_{32}$-NH_2 and Ac-VAIALKAAHYHTHKE-NH_2. The diagrams are calculated from the overall stability constants of the binary complexes and simulate a situation in which equimolar concentrations of all of the chosen ligands and metals are present in a solution.

derived peptide provides a more favorable coordination environment compared to the –HHH– motif present in the CusF fragment. In the calcitermin-derived sequence, Cu(II) can coordinate all three histidines of the HxHxH motif, creating an optimal set of imidazole donors that maximizes stability. By contrast, in Ac-ANEHHHETMSE-NH_2 of CusF, only two histidines participate directly in metal binding, with amide donors completing the coordination sphere. This difference in the number of histidine ligands likely accounts for the lower thermodynamic stability of Cu(II) complexes formed by the –HHH– motif peptide compared to the calcitermin-derived peptide. The opposite situation was observed for complexes with Zn(II) ions (Fig. 8B). In this case, the –HHH– motif peptide exhibits greater stability toward Zn ions than the calcitermin-blocked peptide. This suggests that Zn(II) coordination through three adjacent histidine residues is more favorable than through the HxHxH motif. Zn(II) does not displace a proton from the amide group and can bind to the peptide only *via* imidazole nitrogen atoms, thus the greater distance between two anchoring sites leads to the formation of less stable Zn(II) complexes. A similar situation was previously observed for model sequences Ac-AHHA-NH_2 and Ac-AHAAAHA-NH_2, where the HH motif was more preferred by Cu(II) ions, whereas Zn(II) ions formed more thermodynamically stable complexes with the motif of two histidines separated by three amino acid residues.[35] In addition, Ac-$_{22}$ANEHHHET-MSE$_{32}$-NH_2 carries three acidic residues (two glutamates and one aspartate) located in the immediate vicinity of the binding motif. Such carboxylate groups are frequently involved in Zn(II) coordination in proteins, either as direct ligating atoms or by stabilizing the coordination environment through electrostatic interactions and hydrogen bonding. Their presence may therefore further enhance the stability of Zn(II) complexes with –HHH– motif peptide. By contrast, the calcitermin-derived peptide contains only a single acidic residue, which limits such stabilization and may contribute to the lower affinity of this fragment for Zn(II).

Fluorescence monitoring of metal-induced structural effects in Ac-$_{55}$TIHHDPIAAVNWPEMTMRFTITPQTKMSE$_{83}$-NH_2 *via* the tryptophan residue

The periplasmic metallochaperone CusF has been shown to fine-tune its Cu(I) binding properties through a non-covalent Cu(I)–π interaction with a nearby tryptophan residue, which stabilizes a three-coordinate, solvent-shielded metal site without directly affecting affinity or specificity.[50] Moreover, the study suggests that CusF uses the tryptophan cap to protect against exogenous ligand (O_2) attack while the mechanism of protein–protein complex formation allows the cap to swing out of the way, and thus have minimal effect on the rates of metal transfer.[51] Inspired by this mechanism, the present study investigates how metal binding, specifically of Cu(II) and Zn(II), affects the environment of this single tryptophan residue in the synthetic peptide Ac-$_{55}$TIHHDPIAAVNWPEMTMRFTITPQTKMSE$_{83}$-NH_2. Although direct metal coordination by the indole side chain is not expected, tryptophan fluorescence is highly sensitive to conformational changes, solvent exposure, and nearby quenching centers. Therefore, emission at ~345 nm (upon excitation at 295 nm) was used as a spectroscopic probe of metal-induced structural rearrangements.

Fluorescence emission spectra recorded during titration with Cu(II) and Zn(II) revealed concentration-dependent quenching of the tryptophan emission band (Fig. 9A and B). For both metal ions, progressive addition led to a decrease in fluorescence intensity and a subtle, but consistent, red-shift of the emission maximum. This shift indicates that the tryptophan residue experiences a more polar or more shielded environment upon metal complexation. The quenching is therefore interpreted not as a result of direct coordination, but as a secondary effect of structural reorganization that places the metal ion and its coordination sphere in proximity to the tryptophan residue or alters peptide folding in a way that modulates the local environment of the fluorophore.

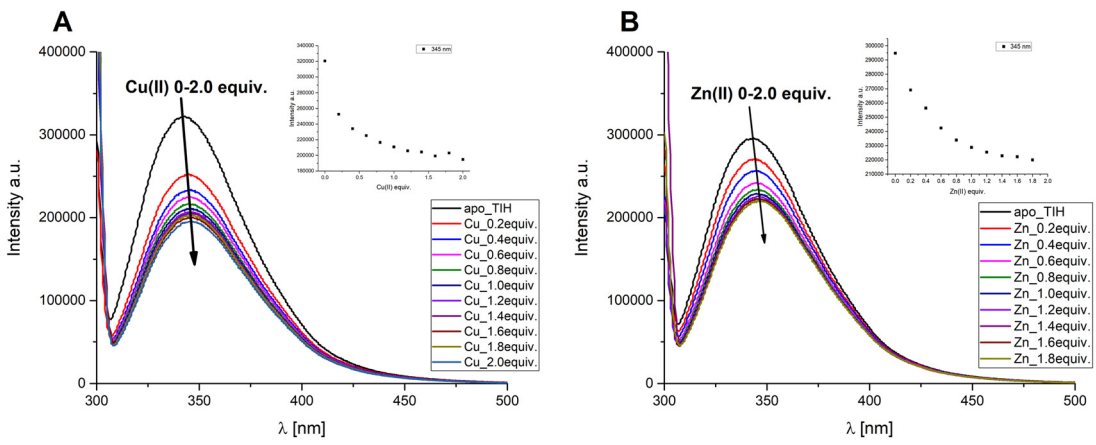

Fig. 9 Fluorescence emission spectra of Ac-$_{55}$TIHHDPIAAVNWPEMTMRFTITPQTKMSE$_{83}$-NH_2 (λ_{ex} = 295 nm) recorded during titration with (A) Cu(II) and (B) Zn(II) in the range of 0–2.0 equivalents. Insets: emission intensity at 345 nm plotted as a function of metal ion equivalents.

Notably, Cu(II) induced a significantly stronger quenching effect than Zn(II), with the emission intensity decreasing sharply at low equivalents and reaching a plateau near 1 : 1 stoichiometry (Fig. 9A). In contrast, the Zn(II)-induced quenching was more gradual and less efficient (Fig. 9B). This distinction is consistent with the paramagnetic nature and high quenching efficiency of Cu(II), as well as potentially stronger or more specific coordination to the peptide backbone or side chains. The subtle red-shift observed for both metal ions further supports the notion of altered local polarity or solvent exposure near the tryptophan moiety.

Taken together, these data demonstrate that both Cu(II) and Zn(II) bind to the peptide and induce conformational changes that affect the environment of the tryptophan residue. The more pronounced effects observed with Cu(II) suggest either stronger binding affinity or a more compact structural rearrangement, leading to more efficient quenching. The use of intrinsic tryptophan fluorescence thus provides a sensitive, non-invasive method to monitor metal-induced structural dynamics in peptides, even in the absence of direct metal–fluorophore interactions.

Conclusions

This work provides a comprehensive characterization of the metal-binding behavior of two metal binding sites from the CusF protein, Ac-$_{22}$ANEHHHETMSE$_{32}$-NH$_2$ and Ac-$_{55}$TIHHDPIAAVNWPEMTMRFTITPQTKMSE$_{83}$-NH$_2$, focusing on their interactions with Cu(II) and Zn(II) ions. Using potentiometry, UV-Vis and CD spectroscopy, mass spectrometry, and steady-state fluorescence distinct preferences in coordination were revealed, depending on both the metal ion and the peptide sequences.

Coordination studies revealed that at physiological pH, both peptides form Cu(II) complexes involving two imidazole nitrogens and one deprotonated amide nitrogen. For Ac-$_{22}$ANEHHHETMSE$_{32}$-NH$_2$, the dominant species is $[CuH_{-1}L]^{2-}$, corresponding to a $[2N_{im}, 1N^-]$ coordination mode. Importantly, this set of donors appears at a lower pH than in the Ac-$_{55}$TIHHDPIAAVNWPEMTMRFTITPQTKMSE$_{83}$-NH$_2$ system, indicating earlier engagement of the backbone amide donor. In contrast, the Met/His-rich metal binding site forms [CuHL] as the major species around pH 7, also with a $[2N_{im}, 1N^-]$ donor set, but with less favorable thermodynamic stability. These results underscore that Ac-$_{22}$ANEHHHETMSE$_{32}$-NH$_2$, despite its shorter sequence, is more efficient at stabilizing Cu(II) coordination under near-neutral conditions, due to the compact –HHH– motif facilitating early amide participation.

In the case of Zn(II), both peptides coordinate through histidine imidazoles, yet Ac-$_{55}$TIHHDPIAAVNWPEMTMRFTITPQTKMSE$_{83}$-NH$_2$ exhibits markedly higher thermodynamic stability of its complexes. Notably, –HHH– motif peptide engages all three histidines in Zn(II) coordination, whereas Met/His-rich metal binding site uses only two. The enhanced stability in Ac-$_{55}$TIHHDPIAAVNWPEMTMRFTITPQTKMSE$_{83}$-NH$_2$ is likely due to its extended sequence offering additional stabilization *via* polar side chains, backbone carbonyls, or a more favorable spatial arrangement for Zn(II)'s preferred tetrahedral geometry. In contrast, the compact arrangement of histidines in Ac-$_{22}$ANEHHHETMSE$_{32}$-NH$_2$ may impose steric constraints that limit Zn(II) affinity, despite the greater number of coordinating residues.

To further probe the structural consequences of metal coordination in the Ac-$_{55}$TIHHDPIAAVNWPEMTMRFTITPQTKMSE$_{83}$-NH$_2$ peptide, steady-state fluorescence measurements targeting its intrinsic tryptophan residue were performed. Titration with both Cu(II) and Zn(II) resulted in progressive quenching of the emission band at ~345 nm, accompanied by a subtle red-shift in the emission maximum. These changes are consistent with metal-induced conformational rearrangements or shielding effects near the tryptophan environment, rather than direct coordination. Quenching was more efficient with Cu(II), suggesting either stronger binding or more compact structural changes that bring the metal center into closer proximity to the fluorophore. This highlights the utility of tryptophan fluorescence as a sensitive probe for detecting local structural changes induced by metal complexation, even in the absence of direct metal–fluorophore interactions.

Finally, comparison with a calcitermin-derived HxHxH peptide reinforced the critical role of histidine spacing: while the compact –HHH– motif in Ac-$_{22}$ANEHHHETMSE$_{32}$-NH$_2$ favored Cu(II) coordination, the more dispersed histidines in the antimicrobial peptide more effectively stabilized Zn(II) complexes.

These findings not only expand the current understanding of CusF's coordination chemistry, but also shed light on how subtle sequence variations can fine-tune metal selectivity at the molecular level. The demonstrated ability of CusF fragments to bind Cu(II), a redox state not typically associated with the protein, highlights a previously underappreciated flexibility in the bacterial copper resistance machinery. Importantly, this work contributes to the broader understanding of bacterial copper homeostasis under oxidative stress, where transient Cu(II) species may become relevant. By dissecting the role of histidine motif architecture in metal preference, this study opens new avenues for designing synthetic metallopeptides and provides a framework for probing the adaptive strategies employed by pathogens to manage toxic metal exposure.

Author contributions

Aleksandra Hecel: conceptualization, investigation (fluorescence, nearCD, MS), formal analysis, writing – original draft, writing – review & editing, supervision, funding acquisition. Michal Pakowski: investigation (potentiometry, CD, UV-Vis), visualization (proposed coordination models).

Conflicts of interest

The authors declare no conflict of interest.

Data availability

The datasets generated and analysed during the current study are available from the corresponding author on reasonable request.

Supplementary information (SI) is available. See DOI: https://doi.org/10.1039/d5dt01770j.

Acknowledgements

This work was supported by the National Science Centre, Poland (grant no. UMO-2023/51/D/ST5/01798).

References

1 A. Giachino and K. Waldron, *Mol. Microbiol.*, 2020, **114**, 377–390.
2 J. Wain, D. House, D. Pickard, G. Dougan and G. Frankel, *Philos. Trans. R. Soc. London, Ser. B*, 2001, **356**, 1027–1034.
3 Y. Fu, F. Chang and D. Giedroc, *Acc. Chem. Res.*, 2014, **47**, 3605–3613.
4 J. Lutkenhaus, *J. Bacteriol.*, 1977, **131**, 631–637.
5 K. Mahendran, E. Hajjar, T. Mach, M. Lovelle, A. Kumar, I. Sousa, E. Spiga, H. Weingart, P. Gameiro, M. Winterhalter and M. Ceccarelli, *J. Phys. Chem. B*, 2010, **114**, 5170–5179.
6 O. Novikova and T. Solovyeva, *Biochem. (Moscow), Suppl. Ser.*, 2009, **3**, 3–15.
7 H. Lee, A. Abdelal, M. Clark and J. Ingraham, *J. Bacteriol.*, 1991, **173**, 5406–5413.
8 S. Bhamidimarri, T. Young, M. Shanmugam, S. Soderholm, A. Basle, D. Bumann and B. van den Berg, *PLoS Biol.*, 2021, **19**, e3001446.
9 L. Novoa-Aponte and J. Argüello, *JBIC, J. Biol. Inorg. Chem.*, 2022, **27**, 509–528.
10 G. Kenney and A. Rosenzweig, *Annu. Rev. Biochem.*, 2018, **87**, 645–676.
11 B. Khalfaoui-Hassani, H. Wu, C. Blaby-Haas, Y. Zhang, F. Sandri, A. Verissimo, H. Koch and F. Daldal, *mBio*, 2018, **9**, DOI: 10.1128/mbio.00065-18.
12 T. Mealman, N. Blackburn and M. McEvoy, *Curr. Top. Membr.*, 2012, **69**, 163–196.
13 F. Long, C. Su, M. Zimmermann, S. Boyken, K. Rajashankar, R. Jernigan and E. Yu, *Nature*, 2010, **467**, 484–488.
14 C. Su, F. Yang, F. Long, D. Reyon, M. Routh, D. Kuo, A. Mokhtari, J. Van Ornam, K. Rabe, J. Hoy, Y. Lee, K. Rajashankar and E. Yu, *J. Mol. Biol.*, 2009, **393**, 342–355.
15 I. Bagai, W. Liu, C. Rensing, N. Blackburn and M. McEvoy, *J. Biol. Chem.*, 2007, **282**, 35695–35702.
16 R. Kulathila, R. Kulathila, M. Indic and B. van den Berg, *PLoS One*, 2011, **6**, e15610.
17 A. Andrei, Y. Öztürk, B. Khalfaoui-Hassani, J. Rauch, D. Marckmann, P. Trasnea, F. Daldal and H. Koch, *Membranes*, 2020, **10**, 242.
18 T. Padilla-Benavides, A. Thompson, M. McEvoy and J. Argüello, *J. Biol. Chem.*, 2014, **289**, 20492–20501.
19 I. Bagai, C. Rensing, N. Blackburn and M. McEvoy, *Biochemistry*, 2008, **47**, 11408–11414.
20 I. Loftin, S. Franke, S. Roberts, A. Weichsel, A. Héroux, W. Montfort, C. Rensing and M. McEvoy, *Biochemistry*, 2005, **44**, 10533–10540.
21 I. Loftin, S. Franke, N. Blackburn and M. Mcevoy, *Protein Sci.*, 2007, **16**, 2287–2293.
22 J. Kittleson, I. Loftin, A. Hausrath, K. Engelhardt, C. Rensing and M. McEvoy, *Biochemistry*, 2006, **45**, 11096–11102.
23 Y. Xue, A. Davis, G. Balakrishnan, J. Stasser, B. Staehlin, P. Focia, T. Spiro, J. Penner-Hahn and T. O'Halloran, *Nat. Chem. Biol.*, 2008, **4**, 107–109.
24 A. Astashkin, A. Raitsimring, F. Walker, C. Rensing and M. McEvoy, *JBIC, J. Biol. Inorg. Chem.*, 2005, **10**, 221–230.
25 A. Vergnes, C. Henry, G. Grassini, L. Loiseau, S. El Hajj, Y. Denis, A. Galinier, D. Vertommen, L. Aussel and B. Ezraty, *PLoS Genet.*, 2022, **18**, e1010382.
26 G. Gran, *Acta Chem. Scand.*, 1950, **4**, 559–577.
27 P. Gans and B. O'Sullivan, *Talanta*, 2000, **51**, 33–37.
28 P. Gans, A. Sabatini and A. Vacca, *Talanta*, 1996, **43**, 1739–1753.
29 L. Alderighi, P. Gans, A. Ienco, D. Peters, A. Sabatini and A. Vacca, *Coord. Chem. Rev.*, 1999, **184**, 311–318.
30 C. F. Baes and R. S. Mesmer, *The Hydrolysis of Cations*, John Wiley & Sons, New York, London, Sydney, Toronto, 1976.
31 G. Arena, R. Cali, E. Rizzarelli and S. Sammartano, *Thermochim. Acta*, 1976, **16**, 315–321.
32 A. Hecel, A. Kola, D. Valensin and D. Witkowska, *Inorg. Chem.*, 2025, **64**, 2936–2950.
33 J. Watly, E. Simonoysky, R. Wieczorek, N. Barbosa, Y. Miller and H. Kozlowski, *Inorg. Chem.*, 2014, **53**, 6675–6683.
34 J. Watly, E. Simonovsky, N. Barbosa, M. Spodzieja, R. Wieczorek, S. Rodziewicz-Motowidlo, Y. Miller and H. Kozlowski, *Inorg. Chem.*, 2015, **54**, 7692–7702.
35 A. Hecel, K. Garstka, H. Kozloeski and M. Rowinska-Zyrek, *J. Inorg. Biochem.*, 2024, **252**, 112456.
36 A. Hecel, J. Watly, M. Rowinska-Zyrek, J. Swiatek-Kozlowska and H. Kozlowski, *JBIC, J. Biol. Inorg. Chem.*, 2018, **23**, 81–90.
37 C. Wilson, M. Karttunen, B. de Groot and V. Gapsys, *J. Chem. Theory Comput.*, 2023, **19**, 7833–7845.
38 A. Norouzy, A. Lazar, M. Karimi-Jafari, R. Firouzi and W. Nau, *Amino Acids*, 2022, **54**, 277–287.
39 D. Wyrzykowski, B. Pilarski, L. Chmurzynski and J. Makowska, *J. Mol. Liq.*, 2020, **312**, 113379.
40 G. Ullmann, *J. Phys. Chem. B*, 2003, **107**, 1263–1271.
41 M. Harms, C. Castañeda, J. Schlessman, G. Sue, D. Isom, B. Cannon and B. García-Moreno, *J. Mol. Biol.*, 2009, **389**, 34–47.
42 P. G. Daniele, E. Prenesti and G. Ostacoli, *J. Chem. Soc., Dalton Trans.*, 1996, 3269–3275.

43 H. Kozlowski, T. Kowalik-Jankowska and M. Jezowska-Bojczuk, *Coord. Chem. Rev.*, 2005, **249**, 2323–2334.
44 L. D. Pettit, S. Pyburn, W. Bal, H. Kozlowski and M. Bataille, *J. Chem. Soc., Dalton Trans.*, 1990, 3565–3570.
45 L. D. Pettit, J. E. Gregor and H. Kozłowski, *Complex Formation between Metal. Ions and Peptides*, JAI Press, London, 1991, vol. 1, pp. 1–41.
46 H. Sigel and R. B. Martin, *Chem. Rev.*, 1982, **82**, 385–426.
47 T. Kowalik-Jankowska, M. Ruta-Dolejsz, K. Wisniewska, L. Lankiewicz and H. Kozlowski, *J. Chem. Soc., Dalton Trans.*, 2000, 4511–4519.
48 D. Witkowska, D. Valensin, M. Rowinska-Zyrek, A. Karafova, W. Kamysz and H. Kozlowski, *J. Inorg. Biochem.*, 2012, **107**, 73–81.
49 M. D'Accolti, D. Bellotti, E. Dzien, C. Leonetti, S. Leveraro, V. Albanese, E. Marzola, R. Guerrini, E. Caselli, M. Rowinska-Zyrek and M. Remelli, *Sci. Rep.*, 2023, **13**, 18228.
50 I. Loftin, N. Blackburn and M. McEvoy, *JBIC, J. Biol. Inorg. Chem.*, 2009, **14**, 905–912.
51 K. Rush, K. Alwan, A. Conner, E. Welch and N. Blackburn, *Inorg. Chem.*, 2024, **63**, 21519–21530.